Cavity alignment using fringe scanning

LIGO SURF Final Report

Laura Paulina Šinkūnaitė

University of Glasgow, United Kingdom

Mentors
Dr. Michael Landry
Dr. Keita Kawabe

17th of September 2015

Abstract

LIGO employs two 4-km long Fabry–Pérot arm cavities, which need to be aligned in order for an interferometer to be locked on a TEM00 mode. Once the cavity is locked, alignment signals can be derived from wave-front sensors which measure the TEM01 mode content. However, the alignment state is not always good enough for locking on TEM00. Even when this is the case, the alignment can be evaluated using a free swinging cavity, that shows flashes when higher-order modes become resonant. By moving test masses, small changes are made to the mirror orientation, and hence the TEM00 mode can be optimised iteratively. Currently, this is a manual procedure, and thus it is very time-consuming. Therefore, this project is aimed to study another possible way to lock the cavity on the TEM00 mode. Misalignment information can also be extracted from the power of the higher-order modes transmitted through the cavity. This report presents an algorithm for this alternative and faster way to derive the alignment state of the arm cavities.

Contents

1 Introduction

1.1 LIGO

LIGO stands for the Laser Interferometer Gravitational-Wave Observatory. There are two identical observatories based approximately 3,000 kilometres apart: one is in Livingston, Louisiana, and its twin is located at the Hanford site, Washington. The Hanford-site Observatory is the one where this project has been carried out. It is required that, if a signal is to be reliably defended as an astrophysical gravitational wave, it must be observed in both observatories. Gravitational-wave signals are so weak that gravitational wave detectors suffer a lot from background noise: strong earthquakes, or cultural noise such as traffic or trains, winds or microseism can negatively impact their performance. Many efforts are put into stabilising system to ensure that those effects are eliminated or reduced to minimum.

The Hanford-site detector is an interferometer which contains two 4 km-long arm cavities formed into "L" shape. The optical configuration of each detector is a suspended, dual-recycled Michelson interferometer with Fabry-Pérot cavities for arms. They need to be aligned, before they can be locked on a fundamental transverse mode, TEM00. Once the cavity is locked, or controlled on resonance, alignment signals can be derived from wave-front sensors which measure the TEM01 mode content, which is a superposition of Hermite-Gaussian TEM01 and TEM10 modes. However, the alignment state is not always good enough for locking on TEM00. Even when this is the case, the alignment can be evaluated using a free swinging cavity, that shows flashes when higher-order modes become resonant. This requires another round of optimisation, which is currently done manually.

1.2 Motivation and objectives

The goal of this project was to derive the alignment state from scanning the cavity length and observing the power build-up of the laser light. By making small changes to the mirror orientation by moving test masses, the TEM00 mode can be optimized iteratively. If the alignment state was derived from scanning the cavity length, this would ease the process of initial alignment. Another goal of the project was to automate the alignment procedure in order to reduce the manual alignment time, i.e. reduce the time to align a given cavity, and increase the reliability and repeatability in doing so.

2 Background theory

2.1 Electric field

An electric field can be described as a sum of the different frequency components and of the different spatial modes:

$$E(t, x, y, z) = \sum_j \sum_{n,m} a_{jnm} u_{nm}(x, y, z) exp(i(\omega_j t - k_j z)),$$

with u_{nm} describing the spatial properties of the beam and a_{jnm} as complex amplitude factors, where ω_j stands for the angular frequency, f is the light field, and the wave-number

$k_j = \omega_j/c$. This notation can be simplified to describe a single frequency component at one moment in time ($t = 0$):

$$E(x, y, z) = exp(-ikz) \sum_{n,m} a_{nm} u_{nm}(x, y, z).$$

2.2   Gaussian beam

A simple laser beam can be described by the Gaussian beam to a good approximation. It can be divided into two different sections along the z-axis: a near field, a region around the beam waist, and a far field, far away from the waist. The length of the near-field region is approximately given by the Rayleigh range, $z_R = \frac{\pi w_0^2}{\lambda}$ (Figure 1).
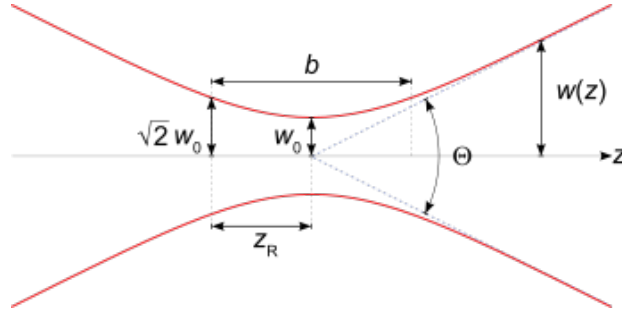
Figure 1: Gaussian beam [1]

Knowing the Rayleigh range, z_R, and the location to the beam waist, $z - z_0$, the following can be calculated:

$$w(z) = w_0 \sqrt{1 + \frac{z - z_0}{z_R}^2} \ .$$

This equation gives the size of the beam along the z-axis. In the far-field regime, where $z \gg z_R, z_9$, it can be approximated by a linear equation:

$$w(z) \approx w_0 \frac{z}{z_R} = \frac{z\lambda}{\pi w_0}.$$

The angle θ between the z-axis and $w(z)$ in the far field is called the diffraction angle, or divergence, and is defined as:

$$\theta = \arctan\left(\frac{w_0}{z_R}\right) = \arctan\left(\frac{\lambda}{\pi w_0}\right) \approx \frac{w_0}{z_R}.$$

2.3   Hermite-Gaussian modes

Hermite-Gaussian modes are the eigenmodes of a general spherical cavity (an optical cavity with spherical mirrors) and represent an exact solution of the paraxial wave equation. One distinguishes between longitudinal modes (along the optical axis) and transverse electromagnetic modes (TEM), the spatial distribution of the light beam perpendicular to

the optical axis. The higher-order Hermite-Gaussian modes can be expressed in terms of the lowest-order mode, u_{00}, which is simply the Gaussian beam:

$$E(x,y,z) = E_0 u_{00} exp(-ikz) = E_0 \left(\frac{1}{R_c(z)} - i\frac{\lambda}{\pi\omega^2(z)} \right)$$

$$\times exp\left(-ik\frac{x^2+y^2}{2R_C(z)} - \frac{x^2+y^2}{\omega^2(z)} - ikz \right)$$

(assuming a single frequency and $t = 0$). Here $R_C(z)$ is the radius of curvature of the beam's wave-front.

The Hermite-Gaussian modes are usually given in their orthonormal form as:

$$u_{nm}(x,y,z) = (2^{n+m+1}n!m!\pi)^{-1/2}\frac{1}{w(z)}exp(i(n+m+1)\Phi(z))$$

$$\times H_n\left(\frac{\sqrt{2}x}{w(z)} \right) H_m\left(\frac{\sqrt{2}y}{w(z)} \right) exp\left(-i\frac{k(x^2+y^2)}{2R_C(z)} - \frac{x^2+y^2}{w^2*(z)} \right),$$

with n, m being the mode indices. In this case n refers to the modes in the $y-z$, or saggital, plane and m to the $x-z$, or tangential, plane. The following functions used in the equation above: $H_n(x)$ - Hermite polynomial of the order n, $w(z)$ - beam radius or spot size, $R_C(z)$ - radius of curvature of the phase front, and $\Phi(z)$ - the Gouy phase.

2.4   Gouy phase-shift

Compared to a plane wave, the Hermite-Gaussian modes have a slightly slower phase velocity, especially close to the waist, in the near-field region. This on-axis longitudinal phase delay is called the Gouy phase:

$$\Phi(z) = \arctan\left(\frac{z-z_0}{z_R} \right).$$

The phase lag ϕ of a Hermite-Gaussian mode is:

$$\phi = (n+m+1)\Phi(z),$$

which is called the Gouy phase-shift.

2.5   Misalignments

In the interferometer, if the optical axes of the beam and the cavity do not overlap perfectly, the set-up is called misaligned. If the beam size or shape at the cavity does not match the beam shape and size of the (resonant) fundamental eigenmode, the beam is then not mode-matched to the cavity [2]. There are four possible types of misalignments of the input axis with respect to the cavity axis: (a) waist size mismatch, (b) axial waist displacement, (c) transverse displacement in the x-direction, and (d) tilt through an angle a_x. Transverse displacements and tilts in the y-direction are equivalent to (c) and (d) [3].
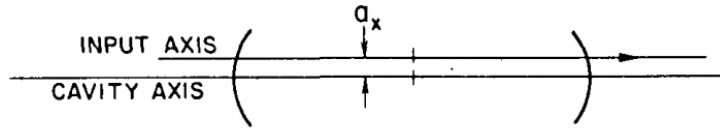
Figure 2: Example of misalignment: transverse displacement [3].
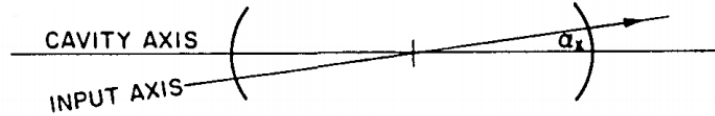
Figure 3: Example of misalignment: tilt through an angle α [3].

Example plots of two types of misalignment are pictured above. Figure 2 shows the transverse displacement and Figure 3 shows the misalignment due to the mirror tilt.

3   Experimental method

3.1   Exposition

In order to develop the algorithm, the work was split into smaller tasks. The first part of the project was to understand modal decomposition coefficients. This was done using MATLAB programming language [4] and a software package called FINESSE [5]. The output of this part was a modal decomposition coefficient table and their ratio table.

The second part of the project was the algorithm development. Gouy phase shift and Gaussian geometry was used together with various statistical techniques to create the output product. The outcome of this part was an algorithm which reads in the power-distribution data, finds the peak values and their positions, takes the ratios of the peak amplitudes with respect to the highest peak, reorders the amplitudes according to their relative positions, and after a procedure of matching to the values from the ratio table from the Simulation part, outputs the normalised misalignment parameter. After the algorithm was developed, further tests were done to improve it and to test its limits.

The objective of the last part of the project was to adapt the algorithm to the real data input from the interferometer. The seven sets of data were collected at the LHO (LIGO Hanford site) X-arm. In order to make the algorithm work, only one region corresponding to single-trip of the data needed to be selected. Since the systematic calibration did not work perfectly, other methods were used to define the data covering the required region of fringe scan. The peak-finding algorithm also needed to be robuster, therefore such functions as "anti-resolution" or "anti-spike" were introduced. And finally, because the

collected data was rough, some data preparation methods such as interpolation and down-sampling were used together with a digital low-pass Butterworth filter to make it readable.

3.2   Software

An initial step of the project included the right choice of the software used to obtain the modal decomposition coefficient table. Two software packages, FINESSE [5] and E2E [6] were considered, with the final choice to use FINESSE due to its ability to perform calculations with the higher-order Hermite-Gaussian modes, because its competitor E2E [6] could only offer the calculations for the fundamental mode HG_{00}. MATLAB was used as a programming language to invoke FINESSE scripts and to produce graphical output.

4   Simulation

4.1   Optical cavity

The starting point for the project was a cavity simulation. In the Finesse [5] simulation software, green TEM00 laser light (532 nm) is injected into the optical system from the end point, i.e. we simulate injecting green light from downstream of the end mass, into the cavity and back towards the input test mass in the corner station. End test mass (ETM) transmits 32% of the initial beam further to the input test mass (ITM). As only 1.1% of the beam passes through the ITM, most of the beam remains inside the cavity and is reflected back and forward multiple times. In a perfectly aligned system, the output beam should have the same transverse mode as the input beam. However, even minimal misalignments of the optics can cause the higher-order Hermite-Gaussian modes to appear. In order to develop an algorithm to minimise the appearance of the higher-order Hermite-Gaussian modes, a simulation of a misaligned system is modelled.
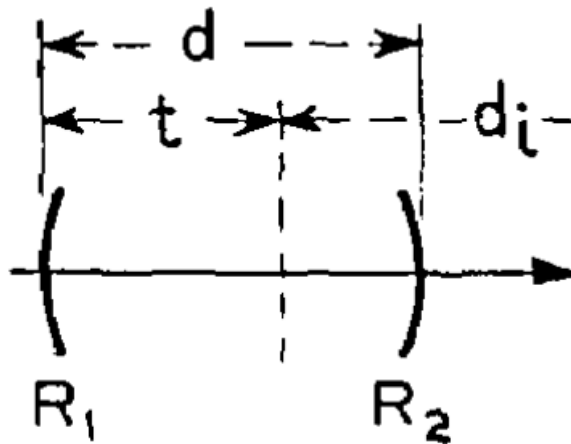
Figure 4: Optical system with two mirrors [7].

Since the laser beam can be approximated as a Gaussian beam, the initial step was to calculate the beam-waist radius and the distance to the beam waist for a simple cavity

with two mirrors with unequal curvatures. The set-up of a cavity is displayed in Figure 4. Using the formula for confocal parameter, b, the beam-waist radius was estimated to be $w_0 = 8.47$ mm.

$$\frac{1}{2}b = \frac{\pi w_0^2}{\lambda} = \frac{\sqrt{d(R_1 - d)(R_2 - d)(R_1 + R_2 - d)}}{R_1 + R_2 - 2d},$$

$$w_0 = \sqrt{\frac{\lambda}{\pi}} \frac{\sqrt[4]{d(R_1 - d)(R_2 - d)(R_1 + R_2 - d)}}{\sqrt{R_1 + R_2 - 2d}}.$$

Another equation from Kogelnik's paper [7] enabled us to calculate the distance to the beam-waist radius, which was found to be $t = 1841.72$ m.

$$t = \frac{d(R_2 - d)}{R_1 + R_2 - 2d}.$$

Here $R_2 = 1939.3$ m and $R_1 = 2241.54$ m are the radii of curvature for the ITM and ETM respectively, and $d = 4000.0$ m is the length of the interferometer arm.

4.2   Set-up

The set-up used to study the modal decomposition coefficients is shown in Figure 5. The laser used emitted 1 W green ($\lambda = 532nm$) light. In this particular simulation only one totally-reflective mirror (ITM) was used that was described by the parameter L, the distance between the laser and the ITM.
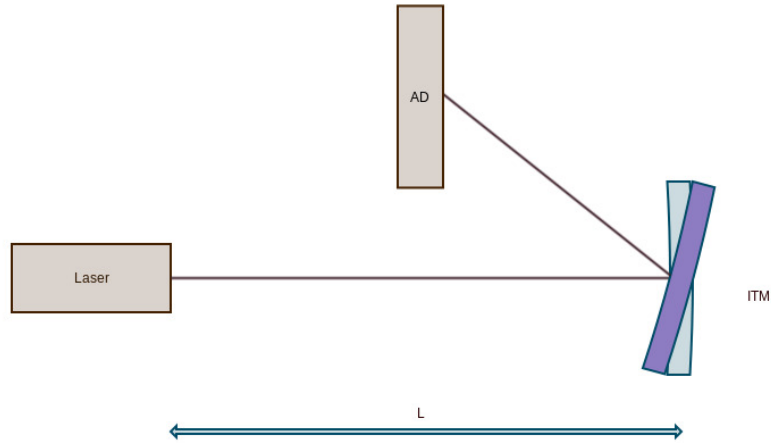
Figure 5: Simulation set-up.

The amplitude detector was placed between the laser and the mirror. It simply plotted the already calculated amplitudes of the light field at the specified frequency. The amplitude at frequency ω_m is a complex number (z), and is calculated as follows:

$$z = \sum_n a_n \text{ with } n | n \in 0, \ldots, N \wedge \omega_n = \omega_m.$$

Here ω_0 is the carrier frequency and $\omega_1, \omega_2, \cdots, \omega_M > 0$ are the sidebands. The result can be written as follows:

$$S = a \exp(i\Phi),$$

with

$$a = \sqrt{\sum_{n,m} |a_{n,m}|^2}, \text{ and } \Phi = \text{phase}\left(\sum_{n,m} a_{n,m}\right).$$

For the sanity check, the photo-detector was placed to the right of the ITM mirror. The intensity at the output port of the photo-detector:

$$|E|^2 = E \times E* = \sum_{i=0}^{N}\sum_{j=0}^{N} a_i a_j^* e^{i(\omega_i - \omega_j)t} = A_0 + A_1 e^{i\overline{\omega_1}t} + A_2 e^{i\overline{omega_2}}t + \cdots,$$

with A_i being the amplitudes of the light power sorted by the beat frequencies $\overline{\omega_i}$. It should be proportional to the square of an amplitude:

$$I \propto a^2.$$

By default the plane-wave approximation was used in FINESSE simulation. The order of the higher-order modes was finite and it was defined by the parameter `maxTEM`: the simulation included higher-order modes TEM_{nm} with $n + m \leq$ `maxTEM` order.

4.3   Decomposition Coefficients

HG_{00} mode is a combination of higher-order Hermite-Gaussian modes.

$$U_{00}(x, y, z) = \sum_{m,n} U_{mn}(x', y', z') a_{mn} \tag{1}$$

Therefore, the first milestone of the project was to study decomposition coefficients, a_{mn}. Initial simulation was written to calculate those coefficients for a light reflected from a flat mirror located at the beam waist. The motive for this particular set-up instead of a usual dual-mirror cavity was based on Finesse limitations.

Because of the geometry of the reflection law, when a flat mirror was located at the beam waist, the total angle of misalignment was $\alpha = 2\theta$, where θ was a tilting angle of the mirror. A plot showing the distribution of the first six TEM modes is shown in Figure 6. Later, the mirror was moved along the z-axis and its curvature was iterated correspondingly to match the wave-front of the beam, i.e. the distance to the mirror, L, was changed from t, which was the distance to the beam waist, to $\approx 10t$.

The x-axis of the plot was a misalignment parameter

$$\left|i\frac{\alpha}{\alpha_0} + \frac{a}{w_0}\right|.$$

But since the radius of the curvature of the mirror was matched to the displacement along the z-axis, the misalignment parameter was simplified to $\left|i\frac{\alpha}{\alpha_0}\right|$. Here α is the misalignment angle.
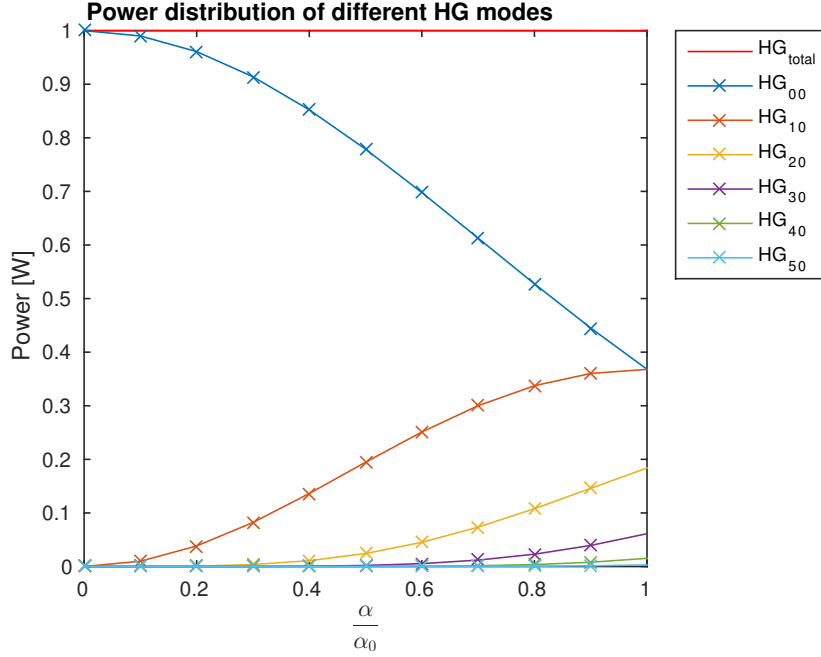
Figure 6: Reflected power distribution of the first six TEM modes for various mirror misalignments.

For R_{ETM} and R_{ITM}, radii of curvatures of the ETM and of the ITM, α can be rewritten as

$$\alpha = \frac{R_{ETM}\theta_{ETM} + R_{ITM}\theta_{ITM}}{R_{ETM}R_{ITM} - L},$$

where α_0 is a divergence angle,

$$\alpha_0 = \sqrt{\frac{\lambda}{\pi}} \sqrt[4]{\frac{(R_{ETM} + R_{ITM} - 2L)^2}{L(R_{ETM} - L)(R_{ITM} - L)(R_{ETM} + R_{ITM} - L)}},$$

a is a tilt, and w_0,

$$w_0 = \sqrt{\frac{\lambda}{\pi}} \sqrt[4]{\frac{L(R_{ETM} - L)(R_{ITM} - L)(R_{ETM} + R_{ITM} - L)}{(R_{ETM} + R_{ITM} - 2L)^2}}$$

is the beam-waist radius. Using the approximations

$$tan(\alpha) \approx \alpha \text{ for a small } \alpha,$$

and

$$\text{when } R_{ITM} \to \infty, \ \frac{R_{ITM} + R_{ETM} - 2L}{R_{ITM} - L} \times \frac{R_{ITM} + R_{ETM} - 2L}{R_{ITM} + R_{ETM} - L} \to 1,$$

the divergence angle becomes

$$\alpha_0 = \sqrt{\frac{\lambda}{\pi}} \sqrt[4]{\frac{1}{L(R_{ETM} - L)}},$$

and the above equation for the x-axis can be derived.

In order for the optical element (ITM mirror in this case) to match the wave-front of the beam, its shape had to be corrected accordingly. Since the location of the mirror was iterated along the z-axis, the radius of its curvature was also iterated:

$$R(L) = L\left[2 + \left(\frac{\pi w_0^2}{\lambda L}\right)\right].$$

Furthermore, in order to compare the plots for different L, the x-axis was normalised using the normalisation constant, θ_C,

$$\theta_C = \sqrt{1 + \left(\frac{\alpha_0}{w_0}\right)^2 (L^2 - (2 \times L \times t) + (t)^2))}.$$
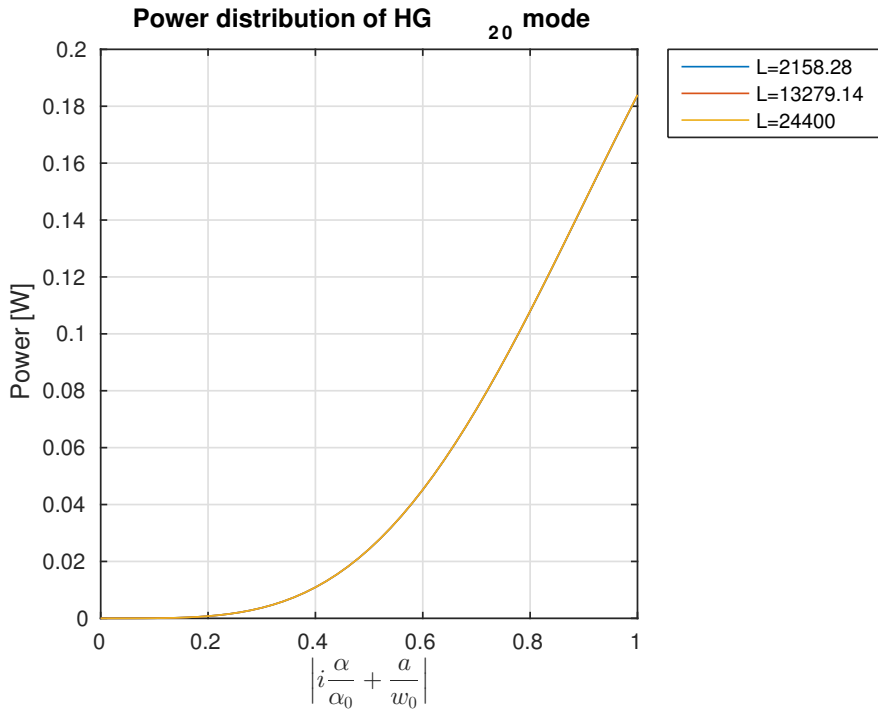
Figure 7: Power distribution of HG_{20} mode for different mirror positions along the z-axis; x-axis normalised.

The power distribution plot is shown in Figure 7. This shows only negligible differences for the mirror placed at different positions, which shows that the normalisation was done correctly. The results of the obtained decomposition coefficients, a_{mn}, for the first 11 higher-order modes (HOM) are laid out in Table 4. The table can be expanded horizontally by including more HOM and vertically by increasing the value of the maximal tilting angle.

5   Algorithm

5.1   Realistic simulation

The second step started with a realistic simulation, which use the original files from the first step as a basis. They were adjusted to reflect the realistic characteristics of the cavity.

Both of the mirrors, ETM and ITM, were used and the cavity length was set to the one which was used at LIGO. In the realistic case both of the mirrors were being tilted, and the output power was studied for different number of TEM modes. A $3-D$ plot of the power distribution of HG_{20} mode is shown in Figure 8.
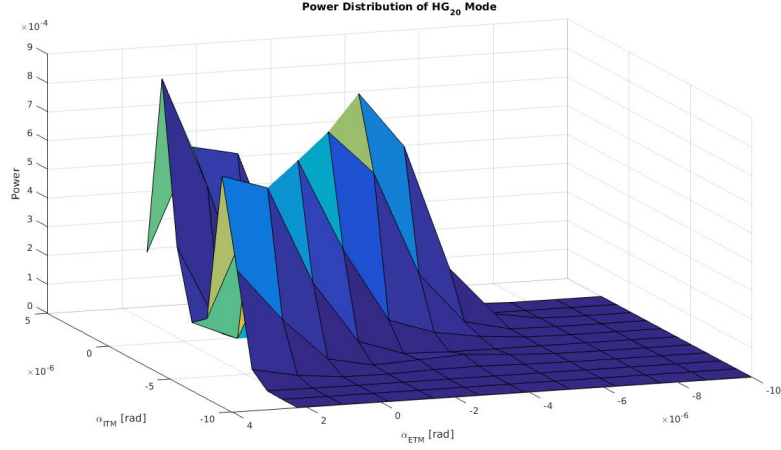
Figure 8: $3-D$ power distribution of HG_{20} mode after misaligning both mirrors.

5.2   Set-up

In the second part of the project, the input is expected to be in the form of a power distribution at a given length, and the algorithm should compare the power and the relative peak heights and should decide about the misalignment parameter

$$\mathcal{O}\left[\left(\frac{a}{w_0}\right)^2 + \left(\frac{\alpha}{\alpha_0}\right)^2\right].$$

Another big challenge in the second step was the extraction of the misalignment information. For the simplicity, this was achieved in stages. The first stage, later called $1-D$ case, only looked at the tilt of one mirror, i.e. if $\alpha_{ITM} \neq 0$ then $\alpha_{ETM} = 0$, and vice versa. The $2-D$ case introduced four angles: both of the ETM and ITM were allowed to move in two directions making pit and yaw rotations. However, if the pit angles were chosen freely, yaw angles for both ETM and ITM were calculated from the relations below, so that one plane would show only transverse displacement, whilst the other plane (perpendicular to the first one) would show the tilt through an angle α. Similar restrictions were applied to the pit angles when yaw angles were chosen freely.

$$\frac{\alpha_Y}{\alpha_0} = \frac{R_{ETM} \cdot \alpha_{ETM} + R_{ITM} \cdot \alpha_{ITM}}{(R_{ETM} + R_{ITM} - L) \times \alpha_0},$$

$$\frac{\alpha_P}{\alpha_0} = \frac{R_{ETM} \cdot \alpha_{ETM} - R_{ITM} \cdot \alpha_{ITM}}{(R_{ETM} + R_{ITM} - L) \times \alpha_0},$$

$$\frac{a}{\omega_0} = \frac{(R_{ETM} - t) \times (R_{ITM} \cdot \alpha_{ITM}) - (t - L + R_{ITM}) \times (R_{ETM} \cdot \alpha_{ETM})}{(R_{ITM} + R_{ETM} - L) \times \omega_0}.$$

And finally, the $3-D$ case corresponded to the case, where both pit- and yaw-angles for both ETM and ITM were chosen freely.

The set-up for this part of the simulation is shown in Figure 9. Here L represents the cavity length, t is the distance to the beam waist, $Rc_{ETM} = 2241.54$ m and $Rc_{ITM} = 1939.3$ m are the radii of the curvatures of the ETM and ITM.
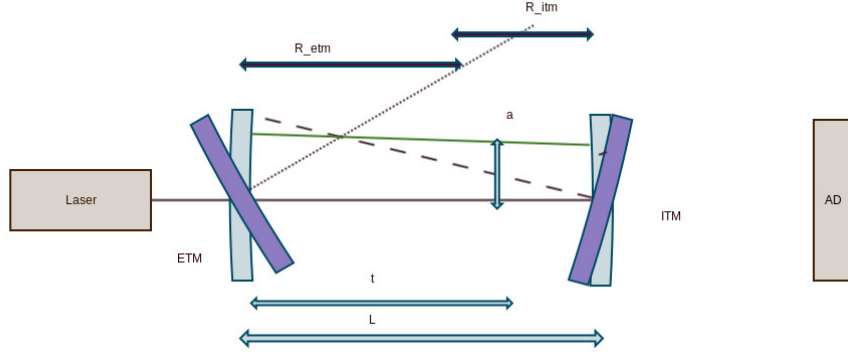
Figure 9: Realistic cavity set-up.

5.3   Development

The idea of the algorithm was to match the peaks found from the fringe scanning to the modal decomposition coefficient data obtained in the first part of the project and to extract the information about the normalised misalignment parameter. In order to do that, the initial struggle needed to overcome was the correct reordering of the peaks.

One of the methods to correctly reorder the peaks in the input data and to match them to the higher-order HG modes, is by using the Gouy phase. The Gouy phase change is evaluated for all TEM modes considered in the simulation, and the relative peak positions are determined using

$$\Phi(m, n; L) = (m + n + 1)\arctan(\lambda L / \pi w_0^2),$$

where (m, n) are the indices of the Hermite-Gaussian modes. Therefore, the field amplitude u becomes:

$$u_{m,n}(r, z) = \frac{w_0}{w} \times H_m\left(\sqrt{2}\frac{x}{w}\right)H_n\left(\sqrt{2}\frac{y}{w}\right)$$
$$\cdot exp\{-i(kz - (m + n + 1)\Phi) - r^2\left(\frac{1}{w^2} + \frac{ik}{2R}\right)\}.$$

Also, the Table 4 is used as a reference table for identification of the misalignment parameters.

The algorithm logic is quite simple. Firstly, the peaks and their locations are found, as shown in Figure 10 and Figure 11. The vector with peak amplitudes is called PKS and with peak locations - LOCS. Then for each row, the ratios with regard to the highest peak
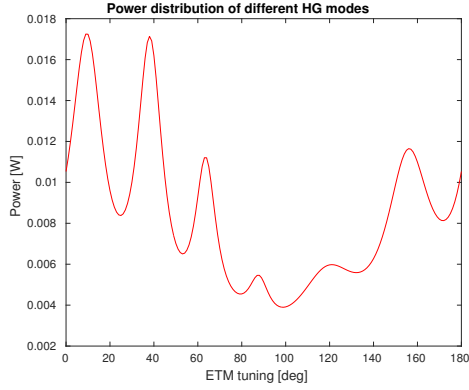
Figure 10: Simulated peaks.
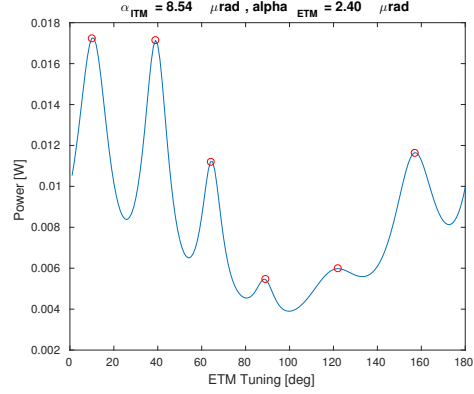
Figure 11: *findpeaks* finds peaks and their locations.

are taken. The peak-ratio vector is called PKR. When this is done, the re-ordering process begins at the PKR element equal to 1, PKR_i. A pre-calculated Gouy phase-shift is added to the right of the LOC_i and to the left. The direction 'to the right' means that the Gouy phase-shift is added and then modulus `mod` 180 is applied, and 'to the left' means that the Gouy phase-shift is subtracted from the LOC_i and then modulus `mod` 180 is applied. After that, the new locations are obtained, LOC_{L2R} and LOC_{R2L}. The minimisation function is used to find the closed element to both of them in the PKR vector: LOC'_{L2R} and LOC'_{R2L}. When those elements are found, the distance between LOC_{L2R} and LOC'_{L2R} and between LOC_{R2L} and LOC'_{R2L} is compared and the shortest is kept. If the shortest distance is 'to the left', i.e.

$$\Delta(LOC_{R2L} - LOC'_{R2L}) < \Delta(LOC_{L2R} - LOC'_{L2R})$$

then the PKR_i corresponding to LOC_{R2L} is added to the maximal PKR_i (or $GOUY\_PKR_i$ on its left side, otherwise - on the right side. The assigned elements are deleted from the remaining list of PKR items, so that re-ordered values would not be repeated. The same is repeated for the edge-most elements until PKR is empty and GOUY_PKR has the same length as original PKR vector. Figure 12 and Figures 13, 14, 15 show the re-ordering procedure.

5.4   Testing

The algorithm was tested using three sets of `maxTEM` = 15, 20, and 25. It was also tested for $1 - D$, $2 - D$, and $3 - D$ cases. The plots Figures 16, 17, 18, and 19 show the limits for the algorithm to extract the correct misalignment parameter. As can be seen from the graphs, the algorithm is the best to describe the normalised misalignment in the region where its values is equal to 0.5 - 2.0. It is guessed that the algorithm does not work when the misalignment is very big because the paraxial approximation does not hold any more.
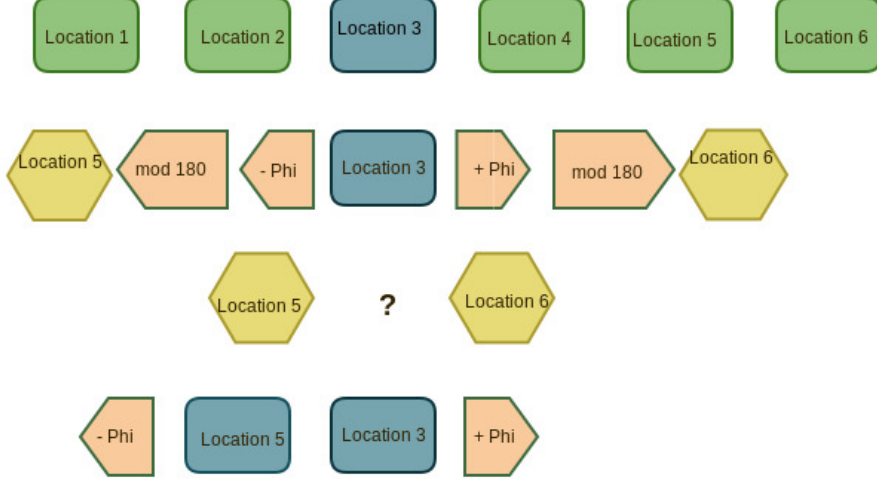
Figure 12: Scheme of the PKR re-ordering.

Another sanity check that was used as a test was a transmittance plot. Transmittance was calculated using the formula:

$$T(\Phi) = T_1 T_2 \frac{1}{|1 - r_1 r_2 e^{0i\Phi}|^2} = \begin{cases} \Phi = 0, \frac{T_1 T_2}{(1-r_1 r_2)^2}, \\ \Phi = \pi, \frac{T_1 T_2}{(1+r_1 r_2)^2}, \end{cases}$$

with r_1 and r_2 being the amplitudes.

$$T_{combined} = P_0 T(\Phi) + P_1 T(\Phi + Gouy) + P_2 T(\Phi + 2 \cdot Gouy)$$
$$+ \cdots + P_{n+m} T(\Phi + (n+m) \cdot Gouy),$$

where `Gouy` meant the Gouy phase shift. If the plot obtained using FINESSE software and pre-calculated transmittance was completely different, those cases were assumed as FINESSE failures and were rejected from the calculation.They would usually correspond to the cases where the combined misalignment parameter was very large. Figure 20 shows a good agreement between FINESSE power distribution and pre-calculated power.

6   Automation

6.1   Data collection

Seven measurements of channel H1_SUS_ETMX_L1_LOCK_L_EXC were carried out. The gain used was 3×10^6 with time of 5 s, Dt = 1, and frequency = 1 Hz. The values calculated from the relative displacements are regarded as the normalised true misalignment parameter, and the deviation between the true and estimated values is obtained at each sample point. Results are shown in Table **??**.
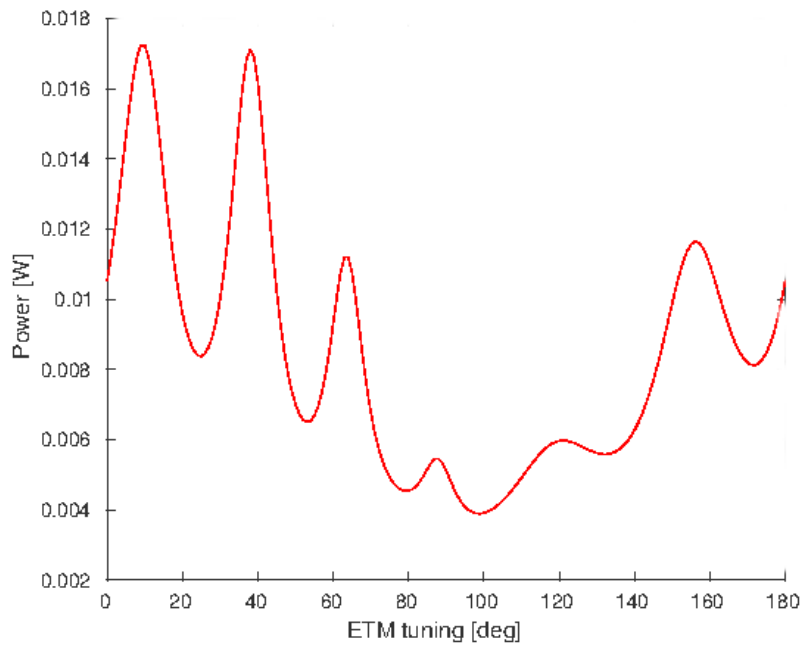
Figure 13: Re-ordering scheme: peak selection.
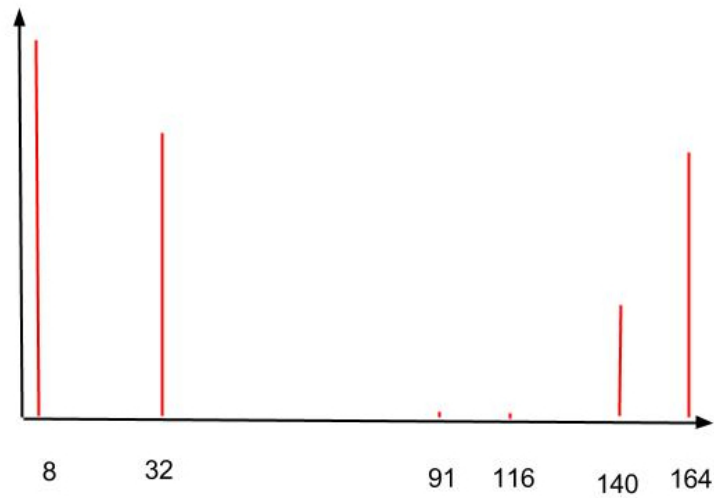
Figure 14: Vectors of peak ratios and their locations, PKR and LOCS.
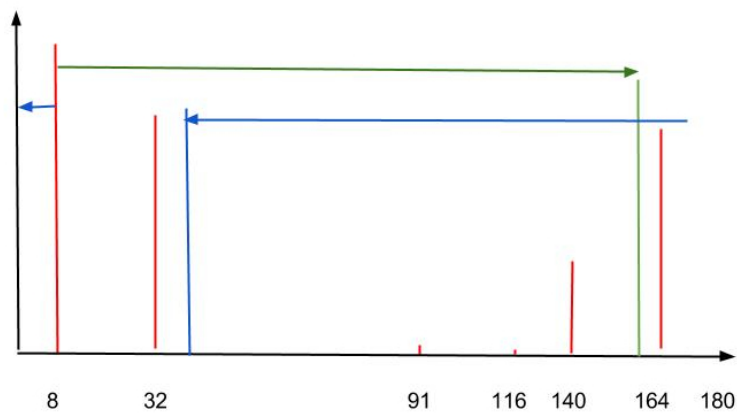
Figure 15: Filling vector GOUY_PKR.
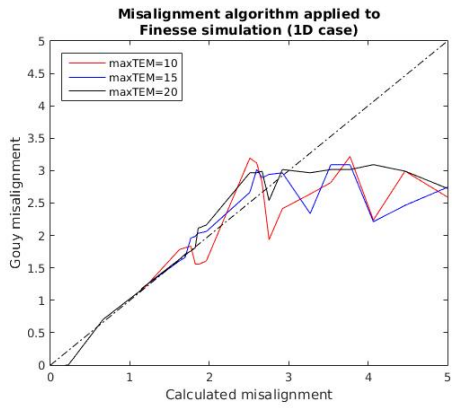
Figure 16: Algorithm testing: 1-D case, maxTEM = 15, 20, 25.
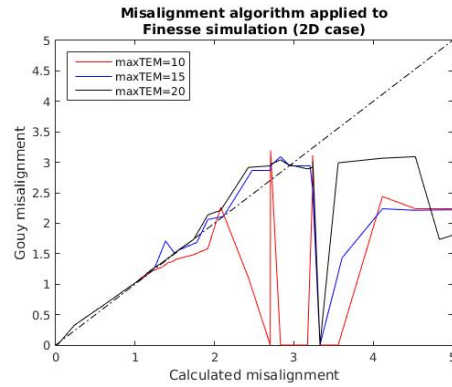
Figure 17: Algorithm testing: 2-D case, maxTEM = 15, 20, 25.
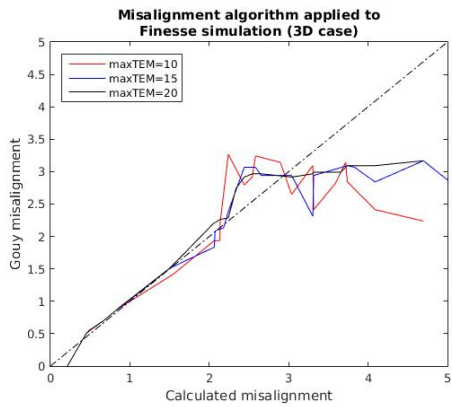
Figure 18: Algorithm testing: 3-D case, maxTEM = 15, 20, 25.
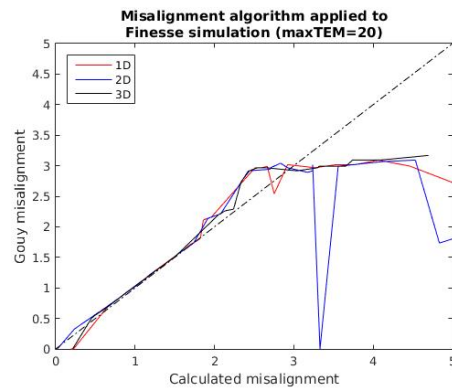
Figure 19: Algorithm testing: maxTEM = 20, 1-D, 2-D, 3-D cases.
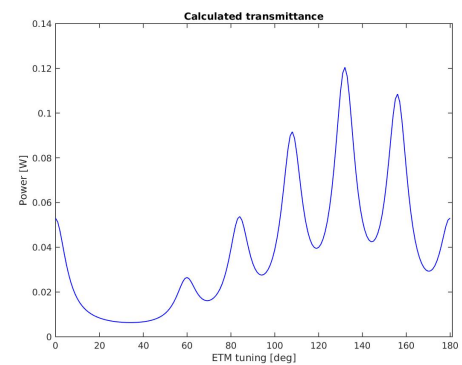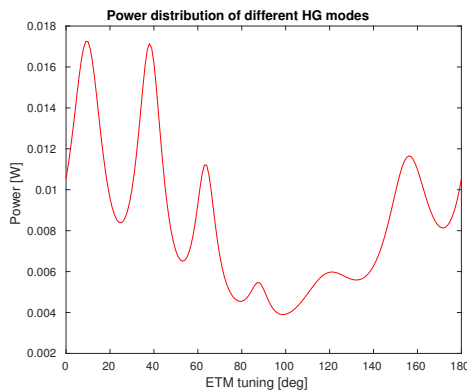
Figure 20: Power calculated with FINESSE and pre-calculated power shows good agreement.

No.	α_{ITM_P}	α_{ITM_Y}	α_{ETM_P}	α_{ETM_Y}	$\Delta\alpha_{ITM\_P}$	$\Delta\alpha_{ITM\_Y}$	$\Delta\alpha_{ETM\_P}$	$\Delta\alpha_{ETM_Y}$	Normalised true misalignment parameter
1	-78.7	1.7	4.8	80.3	0.0	0.0	0.0	0.0	0.000000
2	-76.5	-1.3	6.7	82.5	2.0	-3.0	1.9	2.2	0.687242
3	-74.8	-1.3	8.1	83.6	3.9	-3.0	3.3	3.3	0.903745
4	-74.8	0.0	7.2	81.3	3.9	-1.7	2.4	1.0	0.747380
5	-72.2	-0.3	9.2	81.9	6.5	-2.0	4.4	-8.4	6.405156
6	-70.2	0.4	10.4	81.4	8.5	-1.3	5.6	1.1	1.130984
7	-72.6	3.3	9.5	80.3	6.1	1.6	4.7	0.0	0.945770

Table 1: Green Transmission Measurements.

6.2   Region selection

Since the LIGO calibration was off:

$$\frac{|Witness_{To} - Witness_{From}|}{\lambda} \times 360^o \approx 270^o,$$

which is quite far from 180°, a new method to select the region of interest was used. Power distribution was plotted against the information from witness sensor and the maximal peak was found. Using the Gouy phase-shift, the second highest peak was found which lies in the region where witness sensor is linear, i.e. cavity movement is constant, direction does not change (Figure 21).

6.3   Butterworth filter

Low-pass digital Butterworth filter was used to reduce the number of spikes in the collected data samples and to allow a more accurate selection of the peaks and their locations. Figure 22 shows the Butterworth filter which was applied.

6.4   Order-flip

Information from the witness sensor was used whether to flip the order of the GOUY_PKR or not. If the selected region corresponded to the phase where the cavity was being extended or contracted, the order of the peak-ratio vector was flipped. Otherwise, if the cavity was returning to the relaxed position from previously being extended or contracted, the order of the ratios is not changed. Figure 23 illustrates the case when the order remained the same, whilst Figure ?? shows the case when the order was changed.

6.5   XOR and XNOR gates

XNOR gate is a digital logic gate whose function is the logical complement of the exclusive OR (XOR) gate. The two-input version implements logical equality, behaving according to the truth table to the right. A HIGH output (1) results if both of the inputs to the gate are the same. If one but not both inputs are HIGH (1), a LOW output (0) results.
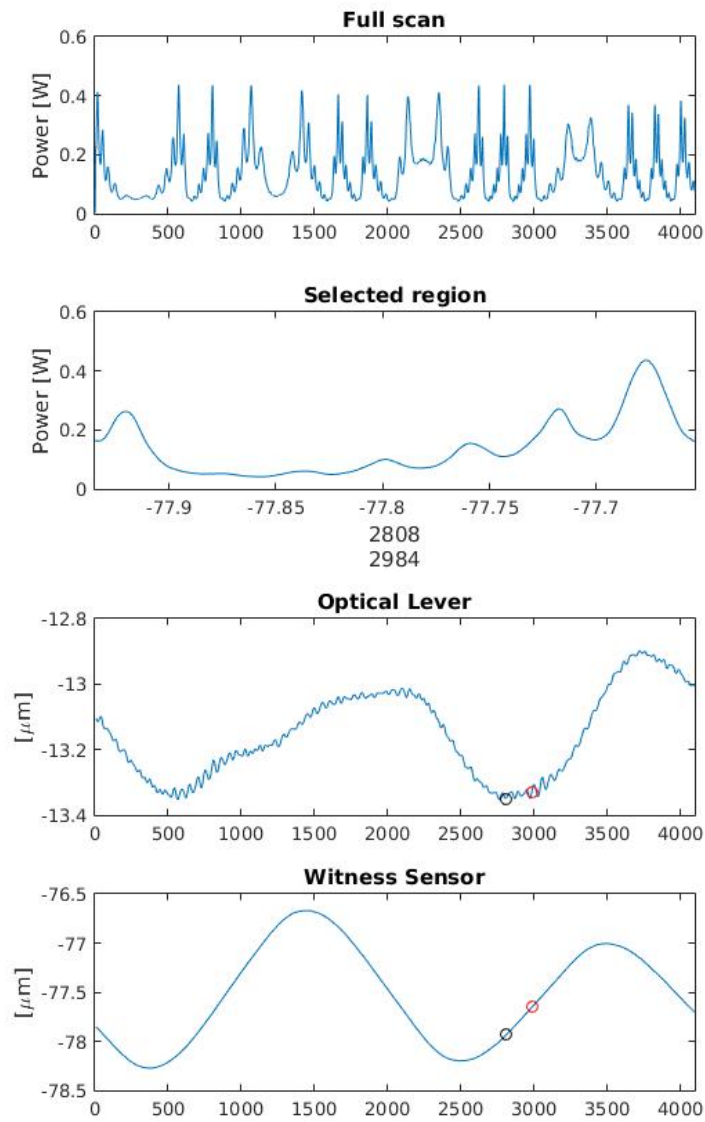
Figure 21: Region selection using the linearity of the witness sensor.

A	B	A XOR B
0	0	0
0	1	1
1	0	1
1	1	0

Table 2: XOR Truth Table.

A	B	A XNOR B
0	0	1
0	1	0
1	0	0
1	1	1

Table 3: XNOR Truth Table.

No	1	2	3	4	5	6	7
True	0	0.687242	0.903745	0.747380	6.4055156	1.130984	0.945770
Algorithm	0.4220	0.8158	1.2096	0.6470	2.8131	0.9002	0.9283
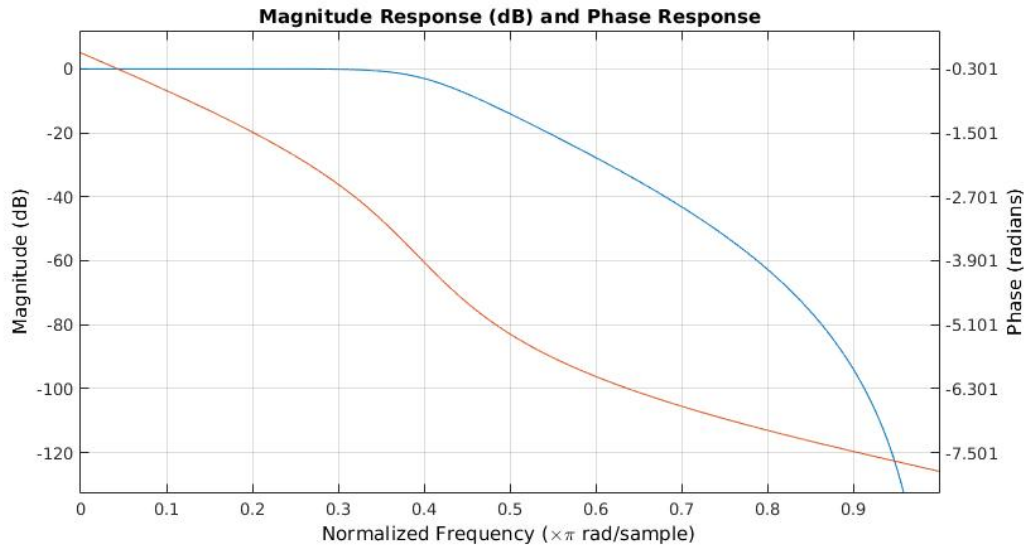
Figure 22: Digital low-pass Butterworth filter with $f_C = 400Hz$, $n = 5$.
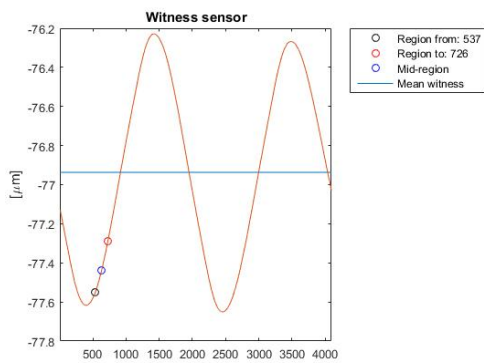
Figure 23: The order of `GOUY_PKR` was not flipped.
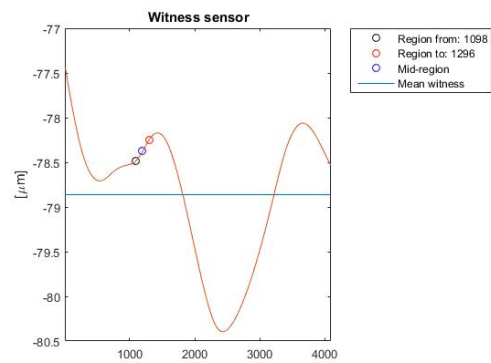
Figure 24: The order of vector `GOUY_PKR` was flipped.

6.6   Results

7   Conclusions

The algorithm developed during this project can accurately extract the information about normalised misalignment parameter within a range between 0.5 and 2.0. During the development stage, two new functions for more robuster peak selection were created: "anti-resolution" (which eliminates peaks that are too close together) and "anti-spike", which calculates the prominence to separate real peaks from the accidental spikes in a dataset. LIGO calibration was found to be off by $\approx 90^o$, therefore a new method to select a single-trip region was used.

The next steps could be the algorithm limit investigation: whether it is due to the paraxial approximation not being held or maybe due to computational issues. Also, an information from the optical-lever sensor could be used to improve the accuracy in the small-misalignment region.

Acknowledgements

A   Mode Decomposition Coefficients

Table 4: Higher-order Hermite-Gaussian mode power coefficients

$\left\|i\frac{\alpha}{\alpha_0} + \frac{a}{w_0}\right\|$	Mode 0	Mode 1	Mode 2	Mode 3	Mode 4	Mode 5	Mode 6	Mode 7	Mode 8	Mode 9	Mode 10
0	1	0	1.7948e-17	0	3.2212e-34	0	5.7814e-51	0	1.0376e-67	0	1.8623e-84
0.020013	0.9996	0.00040012	8.008e-08	1.0685e-11	1.0692e-15	8.5598e-20	5.7105e-24	3.2654e-28	1.6338e-32	7.2666e-37	2.9087e-41
0.040026	0.9984	0.0015986	1.2797e-06	6.83e-10	2.7339e-13	8.7547e-17	2.3362e-20	5.3436e-24	1.0695e-27	1.9026e-31	3.0463e-35
0.060039	0.9964	0.0035896	6.4657e-06	7.7643e-09	6.9927e-12	5.0383e-15	3.0251e-18	1.5568e-21	7.0107e-25	2.8062e-28	1.011e-31
0.080053	0.99362	0.0063636	2.0378e-05	4.3503e-08	6.9653e-11	8.9218e-14	9.5233e-17	8.7131e-20	6.9753e-23	4.9637e-26	3.179e-29
0.10007	0.99004	0.0099073	4.9571e-05	1.6535e-07	4.1367e-10	8.2792e-13	1.3808e-15	1.974e-18	2.4692e-21	2.7455e-24	2.7474e-27
0.12008	0.98569	0.014204	0.00010234	4.9157e-07	1.7709e-09	5.1038e-12	1.2258e-14	2.5233e-17	4.5451e-20	7.2773e-23	1.0487e-25
0.14009	0.98058	0.019233	0.00018861	1.2331e-06	6.0466e-09	2.3719e-11	7.7536e-14	2.1725e-16	5.3264e-19	1.1608e-21	2.2767e-24
0.16011	0.97471	0.02497	0.00031984	2.7312e-06	1.7492e-08	8.9621e-11	3.8265e-13	1.4004e-15	4.4844e-18	1.2764e-20	3.27e-23
0.18012	0.9681	0.031388	0.00050885	5.4994e-06	4.4576e-08	2.8905e-10	1.562e-12	7.2348e-15	2.9321e-17	1.0563e-19	3.4248e-22
0.20013	0.96076	0.038457	0.00076968	1.027e-05	1.0277e-07	8.2272e-10	5.4886e-12	3.1385e-14	1.5704e-16	6.9843e-19	2.7957e-21
0.22014	0.95272	0.046144	0.0011175	1.8041e-05	2.1845e-07	2.1161e-09	1.7081e-11	1.1819e-13	7.1554e-16	3.8507e-18	1.865e-20
0.24016	0.94399	0.054412	0.0015682	3.013e-05	4.3417e-07	5.0051e-09	4.8083e-11	3.9593e-13	2.8527e-15	1.827e-17	1.0531e-19
0.26017	0.93459	0.063222	0.0021384	4.8219e-05	8.1547e-07	1.1033e-08	1.2439e-10	1.2021e-12	1.0165e-14	7.6403e-17	5.1684e-19
0.28018	0.92454	0.072535	0.0028454	7.4411e-05	1.4595e-06	2.29e-08	2.9944e-10	3.3561e-12	3.2913e-14	2.8691e-16	2.2509e-18
0.3002	0.91387	0.082306	0.0037064	0.00011127	2.5053e-06	4.5127e-08	6.7737e-10	8.7152e-12	9.8114e-14	9.8183e-16	8.8426e-18
0.32021	0.9026	0.092491	0.0047389	0.00016187	4.1467e-06	8.4983e-08	1.4514e-09	2.1247e-11	2.7215e-13	3.0986e-15	3.1752e-17
0.34022	0.89076	0.10304	0.0059601	0.00022982	6.6465e-06	1.5377e-07	2.9648e-09	4.8996e-11	7.0848e-13	9.1064e-15	1.0534e-16
0.36024	0.87837	0.11392	0.0073869	0.00031934	1.0354e-05	2.6856e-07	5.8049e-09	1.0755e-10	1.7435e-12	2.5124e-14	3.2583e-16
0.38025	0.86545	0.12506	0.0090356	0.00043522	1.5722e-05	4.5438e-07	1.0943e-08	2.259e-10	4.0803e-12	6.5511e-14	9.4664e-16
0.40026	0.85205	0.13642	0.010921	0.00058289	2.3332e-05	7.4714e-07	1.9938e-08	4.5603e-10	9.127e-12	1.6237e-13	2.5998e-15
0.42028	0.83818	0.14796	0.013059	0.00076841	3.391e-05	1.1972e-06	3.5222e-08	8.8822e-10	1.9599e-11	3.8441e-13	6.7857e-15
0.44029	0.82388	0.15961	0.015461	0.00099847	4.836e-05	1.8738e-06	6.0504e-08	1.6745e-09	4.0552e-11	8.7292e-13	1.6912e-14
0.4603	0.80917	0.17134	0.01814	0.0012804	6.778e-05	2.8705e-06	1.013e-07	3.0644e-09	8.1109e-11	1.9083e-12	4.0408e-14
0.48032	0.79409	0.18309	0.021106	0.0016221	9.3498e-05	4.3114e-06	1.6567e-07	5.4568e-09	1.5727e-10	4.0288e-12	9.2889e-14
0.50033	0.77866	0.1948	0.024367	0.002032	0.00012709	6.359e-06	2.6514e-07	9.476e-09	2.9633e-10	8.2372e-12	2.0607e-13
0.52034	0.76293	0.20644	0.02793	0.0025192	0.00017042	9.2226e-06	4.1592e-07	1.6078e-08	5.4381e-10	1.635e-11	4.4241e-13
0.54035	0.74692	0.21795	0.0318	0.0030931	0.00022544	1.3169e-05	6.4045e-07	2.6698e-08	9.7382e-10	3.1574e-11	9.2133e-13
0.56037	0.73065	0.22929	0.035978	0.0037635	0.00029527	1.8532e-05	9.6929e-07	4.3455e-08	1.7046e-09	5.9438e-11	1.8653e-12
0.58038	0.71417	0.24041	0.040466	0.0045408	0.00038214	2.5729e-05	1.4435e-06	6.942e-08	2.9212e-09	1.0926e-10	3.6782e-12
0.60039	0.6975	0.25128	0.045261	0.0054351	0.0004895	3.5269e-05	2.1176e-06	1.0898e-07	4.9076e-09	1.9644e-10	7.0768e-12
0.62041	0.68068	0.26183	0.05036	0.0064573	0.00062098	4.7774e-05	3.0629e-06	1.6831e-07	8.0931e-09	3.4591e-10	1.3306e-11
0.64042	0.66373	0.27205	0.055755	0.0076178	0.0007806	6.3992e-05	4.3716e-06	2.5598e-07	1.3115e-08	5.973e-10	2.4483e-11
0.66043	0.64668	0.28189	0.061439	0.0089271	0.00097284	8.4813e-05	6.1617e-06	3.837e-07	2.0907e-08	1.0126e-09	4.4141e-11
0.68045	0.62957	0.29132	0.067399	0.010396	0.0012026	0.00011129	8.5829e-06	5.6736e-07	3.2816e-08	1.6872e-09	7.8071e-11
0.70046	0.61242	0.30029	0.073623	0.012034	0.0014751	0.00014466	1.1823e-05	8.2816e-07	5.076e-08	2.7655e-09	1.3561e-10
0.72047	0.59526	0.3088	0.080096	0.01385	0.0017962	0.00018637	1.6113e-05	1.1941e-06	7.7434e-08	4.4633e-09	2.3154e-10
0.74049	0.57811	0.3168	0.0868	0.015855	0.0021721	0.00023805	2.1741e-05	1.702e-06	1.1658e-07	7.0983e-09	3.8897e-10
0.7605	0.56102	0.32427	0.093715	0.018056	0.0026091	0.00030161	2.9055e-05	2.3992e-06	1.7334e-07	1.1132e-08	6.4345e-10
0.78051	0.54399	0.33119	0.10082	0.020461	0.0031142	0.0003792	3.8478e-05	3.3466e-06	2.5469e-07	1.7229e-08	1.0489e-09
0.80053	0.52706	0.33755	0.10809	0.023076	0.0036947	0.00047325	5.0515e-05	4.6218e-06	3.7e-07	2.633e-08	1.6863e-09
0.82054	0.51024	0.34333	0.11551	0.025907	0.004358	0.00058648	6.577e-05	6.3221e-06	5.3175e-07	3.9755e-08	2.675e-09
0.84055	0.49357	0.34851	0.12304	0.028959	0.0051119	0.0007219	8.4955e-05	8.5694e-06	7.5635e-07	5.9339e-08	4.1899e-09
0.86056	0.47706	0.35308	0.13066	0.032234	0.0059643	0.00088286	0.0001089	1.1514e-05	1.0653e-06	8.7601e-08	6.4835e-09
0.88058	0.46073	0.35704	0.13834	0.035736	0.0069233	0.001073	0.00013859	1.5343e-05	1.4862e-06	1.2797e-07	9.9168e-09
0.90059	0.44461	0.36038	0.14606	0.039463	0.0079968	0.0012964	0.00017514	2.028e-05	2.0548e-06	1.8506e-07	1.5e-08
0.9206	0.4287	0.36311	0.15377	0.043415	0.0091931	0.0015573	0.00021984	2.66e-05	2.8162e-06	2.6504e-07	2.2448e-08
0.94062	0.41304	0.36521	0.16146	0.04759	0.01052	0.0018604	0.00027416	3.4632e-05	3.8277e-06	3.7606e-07	3.3252e-08
0.96063	0.39763	0.36671	0.1691	0.051983	0.011985	0.0022107	0.00033979	4.4768e-05	5.1608e-06	5.2884e-07	4.8772e-08
0.98064	0.38248	0.36759	0.17664	0.056588	0.013596	0.0026134	0.00041861	5.7474e-05	6.9045e-06	7.3731e-07	7.086e-08
1.0007	0.36762	0.36788	0.18407	0.061399	0.01536	0.0030742	0.00051273	7.3298e-05	9.1687e-06	1.0195e-06	1.0202e-07

B   Code

Full collection of scripts used in the project can be downloaded from `https://github.com/lsinkunaite/Cavity_Alignment/blob/master/Project.zip`.

References

[1] *Gaussian beam*, `https://upload.wikimedia.org/wikipedia/commons/thumb/5/53/ GaussianBeamWaist.svg/416px-GaussianBeamWaist.svg.png`.

[2] Y. Hefetz, N. Mavalvala, and D. Sigg, *Principles of calculating alignment signals in complex resonant optical interferometers*, J. Opt. Soc. Am. B **14 (7)**, 1597-1605 (Jul 1997).

[3] D. Anderson, *Alignment of resonant optical cavities*, Appl. Opt. **23 (17)**, 2944-2949 (1984).

[4] *MATLAB*, `http://www.mathworks.com/?refresh=true`.

[5] *Finesse manual*, `http://www.gwoptics.org/finesse/`.

[6] *E2E software*, `http://www.ligo.caltech.edu/~e2e/`.

[7] H. Kogelnik and T. Li, *Laser beams and resonators*, Appl. Opt. **5 (10)**, 1550-1567 (1966).

[8] P.Fulda, *Precision Interferometry in a New Shape: Higher-order Laguerre-Gauss Modes for Gravitational Wave Detection*, Springer (2014).

[9] *Numerical modelling tools for GW detectors*, `https://gwic.ligo.org/simulations/`.